

Analyzing the dynamic performance of hybrid reluctance actuators for feedback control

Christian Haider, Ernst Csencsics, and Georg Schitter

Abstract—This paper presents a comparative analysis of hybrid reluctance actuators (HRAs), one with a solid core and a version with a layered core, respectively. The dynamic performance is evaluated by employing flux control and current control for both actuators. With flux control, the phase lag caused by eddy current diffusion in the solid yoke HRA is reduced by 41° at the suspension mode as compared to current control. This enables the implementation of a cascaded control structure, with H_∞ position control reaching a closed-loop bandwidth of 750 Hz for the solid core HRA, similar to the conventional approach using a current-controlled laminated actuator. This offers the option to dispense yoke lamination in favor of easier manufacturing and increased yoke fill factor.

I. INTRODUCTION

In many fields of modern industry, high-precision motion is needed for manufacturing and metrology applications [1]. Electromagnetic voice coil actuators (VCAs) exploiting the Lorentz force are often employed for this purpose [2], as they feature high linearity and a comparably long working range, while delivering a position-independent force, known as zero-stiffness property [3]. These actuators are used for precision machining [4], multiaxis scanning devices [3], fast steering mirrors (FSMs) [5] and active sample-tracking measurement platforms [6]. However, the force-to-current ratio (i.e., motor constant) of these actuators is relatively small [2]. Consequently, a high current is required to achieve the necessary high acceleration, required for a high-speed movement or scanning operation. Moreover, the resistive heating of the actuator can also impair the system performance [7].

In reluctance actuators, the force-to-current relation is quadratic, meaning a higher force density can be achieved with less heat dissipation [8]. However, the highly non-linear force-to-current relationship, the magnetic hysteresis and a high position-dependence need to be compensated [9].

In a hybrid reluctance actuator (HRA), actuation coils and permanent magnets are combined to generate magnetic flux in a ferromagnetic yoke, again resulting in a linear force-to-current relationship and realising a motor constant several times higher than conventional VCAs [2]. HRAs have been successfully integrated in FSMs [10], tool servos [11] and vibration isolation systems [12]. The achievable force is, however, position-dependent, as the biasing flux of the permanent

magnet entails a negative stiffness in the system. By attaching a tailored positive stiffness to the mover, e.g. leaf springs or flexure beams, the negative stiffness can be counteracted around the equilibrium point, achieving open-loop stability [13]. Additionally, a HRA shows inherent non-linearities due to magnetic hysteresis and eddy currents in the actuator yoke, which are caused by the changing magnetic field due to currents applied to the actuation coils, leading to a bandwidth-limiting phase lag with increasing frequency [14]. Eddy current formation can be limited either by substituting the steel core with special material, which offers a high permeability and a high specific electric resistance [14] or by manufacturing the actuator yoke out of laminated steel sheets with insulating layers in between [15]. With shrinking yoke geometry, however, the achievable performance of laminated-core HRAs is limited, if the sheet thickness approaches the insulating layer thickness. Essentially, less cross-section area remains to guide magnetic flux, meaning that the effective fill factor decreases. This, in turn, limits the achievable mover force, resulting in a reduced motor constant. By using a solid-core HRA, the whole cross-section area can be used to guide magnetic flux while the avoidance of yoke lamination lifts the restriction to single 2D geometries, enabling advanced actuator layouts. In current-controlled HRAs, actuator non-linearities resulting from hysteresis and phase lag due to eddy currents cannot be compensated by feedback control. As a remedy, flux control can be used, as the magnetic non-linearities show up in the flux measurement and can therefore be rejected by flux feedback control [13]. It remains, however, unclear how and to which extent flux control can reduce the phase lag resulting from eddy current formation.

The contribution of this paper is the analysis of the system dynamics of hybrid reluctance actuators for laminated and a solid yoke configuration. Particularly, the influence of the sensing and control configuration on the achievable control bandwidth is analysed, thereby offering valuable design guidance for future HRA concepts.

II. SYSTEM DESIGN

In order to explore the dynamic properties of a solid core HRA and facilitate a meaningful comparison with a state-of-the-art layered core, this section presents the development of these two actuator types. For both actuators, the same steel type (EN10025-S235JR) is used, which has a residual magnetization of $B_r = 1.34\text{T}$ and a maximum relative permeability of $\mu_{r,max} = 2400$ [16]. In Fig. 1, the setup of the solid core actuator type is depicted. Two identical actuation coils are

The authors are at the Automation and Control Institute (ACIN), TU Wien, Gusshausstrasse 27-29, 1040 Vienna, Austria. Corresponding author: haider@acin.tuwien.ac.at

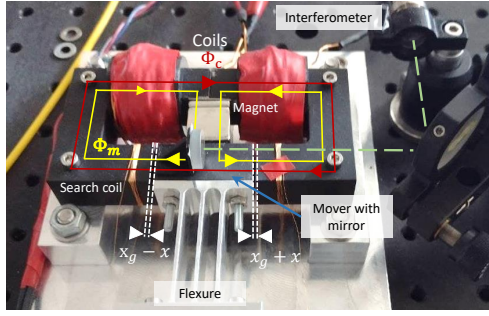


Fig. 1: Experimental setup of the solid-core actuator with indicated flux paths of coil flux Φ_c and magnet flux Φ_m and shown left and right air gaps $x_g \pm x$.

connected in series and attached to a custom-made power amplifier with an integrated shunt resistor to measure the coil current. The ferromagnetic mover with the mirror is guided by an aluminium flexure, which adds a positive stiffness to the system and is designed for a specific suspension mode with a resonance frequency of 193 Hz [13]. The mover motion is observed with an interferometric sensor (IDS3010, Attocube Systems AG, Germany). In order to enable a flux measurement, the voltage induced in a search coil is measured and amplified with an instrumentation amplifier (INA126U, Texas Instruments, USA). A gaussmeter (G-08, Hirst Magnetics, UK) is used to measure the flux density in the airgap. The measured flux and current signals are read via 16-bit ADCs connected to a field-programmable gate array (FPGA) (DS5203, dSpace GmbH, Germany) with a sampling frequency of 10 MHz. The interferometer signal is processed in a rapid prototyping platform (DS1005, dSpace) featuring a sampling frequency of 20 kHz. The specifications of the setup are summarized in Tab. I.

In order to determine the flux in the stator yoke, the induced voltage in the search coil is measured and via Faraday's law [2] the flux linkage can be derived as

$$\hat{\Phi} = \frac{1}{s} \frac{1}{N_{\text{coil}}} g_{IA} \hat{U}_{\text{coil}} \quad (1)$$

in the Laplace domain with a multiplicative instrumentation amplifier gain g_{IA} and the coil windings N_{coil} . The integrator causes a drift in the output signal due to integration of low-frequency bias noise. Therefore, sensor fusion is implemented for flux measurement by using a complementary filter structure, consisting of a high-pass filter for the search coil signal and a low-pass filter for the current monitor signal. Corner frequencies of $\omega_c = 10$ Hz are experimentally determined to filter out low-frequency noise of the search coil. Up to ω_c , the current monitor signal U_{cur} is used for feedback control. For higher frequencies, the amplified coil voltage U_{flux} is integrated and fed back to the controller. In order to correctly add the two signals, multiplicative filter gains g_s and g_c are added. The sensor fusion filter structure is depicted in Fig. 2.

III. SYSTEM MODELLING

In an HRA, the magnetic biasing flux Φ_m of a permanent magnet is superimposed with the steering flux Φ_c of the

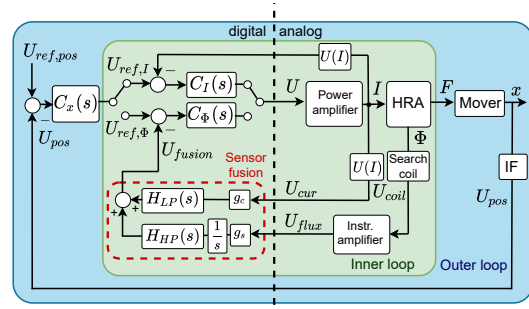


Fig. 2: Block structure of the control system with the flux controller $C_\Phi(s)$ and the current controller $C_I(s)$.

TABLE I: Parameters of both experimental actuators.

Parameter	Symbol	Value
Half-width of yoke	b	7.5 mm
Cross-section area	$A = 4b^2$	15 mm \times 15 mm
Coercitivity	H_c	1 MA/m
Air gaps	x_g, l_f	1 mm
Magnet length	l_m	19 mm
Coil windings	N	120
Search coil windings	N_{coil}	16
Path-length in yoke	l	270 mm
Conductivity	σ	1.82×10^6 S/m

actuation coils. The flux paths inside the ferromagnetic yoke are illustrated in Fig. 1. The permanent magnet's flux serves as a magnetic pre-load, enabling a proportional relationship between coil current and the actuation force on the mover. For modelling the magnetic circuit, the permeability of the yoke is assumed to be large enough to neglect the magnetic reluctance of the yoke itself. The fluxes across the left and right air gap can be described as

$$\Phi_l = \Phi_c + \Phi_m \frac{R_r}{R_l + R_r} = \Phi_v + \frac{1}{2} \Phi_m, \quad (2)$$

$$\Phi_r = \Phi_c - \Phi_m \frac{R_l}{R_l + R_r} = \Phi_v - \frac{1}{2} \Phi_m \quad (3)$$

with the reluctances R_r , R_l and by using a variable flux component [13]

$$\Phi_v(x, I) = \Phi_c + \Phi_m \frac{x}{2x_g}. \quad (4)$$

The force F acting on the mover is derived by using the Maxwell stress tensor and results to [17]

$$F = \frac{\Phi_l^2 - \Phi_r^2}{2\mu_0 A} = \frac{1}{2\mu_0 A} \Phi_m \Phi_v = K_{mf} \Phi_v, \quad (5)$$

indicating the direct proportionality between F and Φ_v . Substituting for Φ_m and Φ_v and assuming the magnet length l_m is sufficiently larger than the length of the air gap l_f , the equation above can also be expressed by

$$F = \underbrace{\frac{2\mu_0 AN H_c l_m}{2l_m x_g + x_g^2 - x^2} I}_{K_{mc}(x)} + \underbrace{\frac{2\mu_0 A H_c^2 l_m^2 x_g}{(2l_m x_g + x_g^2 - x^2)^2} x}_{k_a(x)} \quad (6)$$

with a motor constant $K_{mc}(x)$ and an actuator stiffness $k_a(x)$, indicating the position-dependent negative stiffness of the actu-

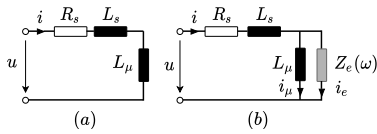


Fig. 3: Equivalent circuits of magnetized solid-core without (a) and with eddy currents (b).

ator [13]. By adding a positive stiffness to stabilize the mover around the center position, the system can be described as a lumped mass-spring-damper model with the equation of motion for the magnetic force F acting on the mover

$$F = m\ddot{x} + c\dot{x} + kx, \quad (7)$$

with the mover's mass m , the flexure stiffness k and a damping coefficient c . With Eq. 5, 6 and 7, the set of dynamic equations of the hybrid reluctance actuator can then be written in the Laplace domain as

$$\frac{x(s)}{I(s)} = \frac{K_{mc}(x)}{ms^2 + cs + (k - k_a(x))}, \quad (8)$$

$$\frac{x(s)}{\Phi_v(s)} = \frac{K_{mf}}{ms^2 + cs + k}. \quad (9)$$

Using current-feedback control, the non-linearities in K_{mc} impair the control performance. Additionally, hysteresis causes a phase offset between input current and magnetic flux, which cannot be compensated by current feedback control [18]. The same applies for non-linearities arising from eddy current formation [13]. In contrast, Eq. 9 highlights the advantage of flux control: By directly measuring and controlling the variable flux Φ_v , the position-dependency and the impact of non-linearities show in the measured flux of Eq. 4 and can be included in the control input.

A. Impact of eddy currents

In order to model the effects of eddy currents on the dynamic system behaviour, the complex actuator impedance can be expressed as

$$\tilde{Z} = R_s + j\omega(L_s + L_\mu) = R_s + j\omega L, \quad (10)$$

with the wire resistance R_s and the actuator inductance L , comprising of a leakage inductance L_s and a magnetizing inductance L_μ due to the iron core, as shown in Fig. 3a. This simple form, however, is only valid for a uniform current density inside the actuation coils and a uniform magnetic field distribution in the yoke, when omitting the effects of eddy currents. This is a viable assumption for a dynamically operated layered core actuator and also for a solid core in quasi-static operation, such that the transfer function from a power amplifier's input reference U to the resulting actuator current I can be expressed as

$$P_{I,\text{layered}}(s) = \frac{I(s)}{U(s)} = \frac{g_{amp}}{R_s + sL} \quad (11)$$

with an amplifier gain g_{amp} . The measured response is depicted in Fig. 4a. The pole resulting from the inductance introduces a characteristic low-pass system behaviour, which can be compensated by a PI-feedback controller [19].

In the case of a dynamically operated solid yoke, the alternating

magnetic field created by the actuation current induces eddy currents, which in turn are responsible for the formation of an opposing magnetic field, which counteracts the magnetizing field. The resulting field distribution shows a larger magnetic field density closer to the surface of the yoke and a field weakening in the yoke center, referred to as magnetic skin effect [20]. The field distribution inside the yoke is therefore dependent on the geometric properties of the actuator.

Eddy currents can be modelled as a current i_e flowing in parallel to the magnetizing inductance L_μ over an impedance $Z_e(\omega)$ in the equivalent circuit [21], [22], as depicted in Fig. 3b. The magnetic skin effect is considered by $Z_e(\omega)$, which is proportional to the square root of the frequency ω . In order to model this influence an approximation can be used to relate the flux Φ inside a solid yoke with an applied current I . Taking into account the half-width of the actuator yoke b , the flux path length l and the break frequency [23]

$$\omega_b = 1/(g_1 b^2 \sigma \mu_0 \mu_r) \quad (12)$$

with a gain g_1 , the transfer function can be written as

$$\Lambda_{\Phi,\text{solid}}(\omega) = \frac{\Phi(\omega)}{I(\omega)} \approx g_2 \frac{\mu_0 \mu_r N}{l} \left(\frac{4b^2}{1 + \sqrt{j\omega/\omega_b}} \right). \quad (13)$$

As depicted in the magnitude plot of Fig. 4a, this model accurately describes the flux-to-current relationship in a solid yoke up to about 1 kHz, when compared to the flux measurement $\Psi_{\Phi,\text{solid}}$, conducted with a gauss meter in the actuator's air gap. The modelled behaviour deviates slightly from the measured data, as the relative permeability μ_r appears both in $\Lambda_{\Phi,\text{solid}}$ and ω_b , but is in general not constant and depends on the driving frequency and the magnetic field strength, which has to be considered when using this model.

The proportional relationship of Eq. 13 to $1/\sqrt{\omega}$ translates to the -10 dB/dec slope shown in the bode plot. This behaviour can also be seen in the measured transfer function of $P_{I,\text{solid}}$, showing the impact of eddy currents.

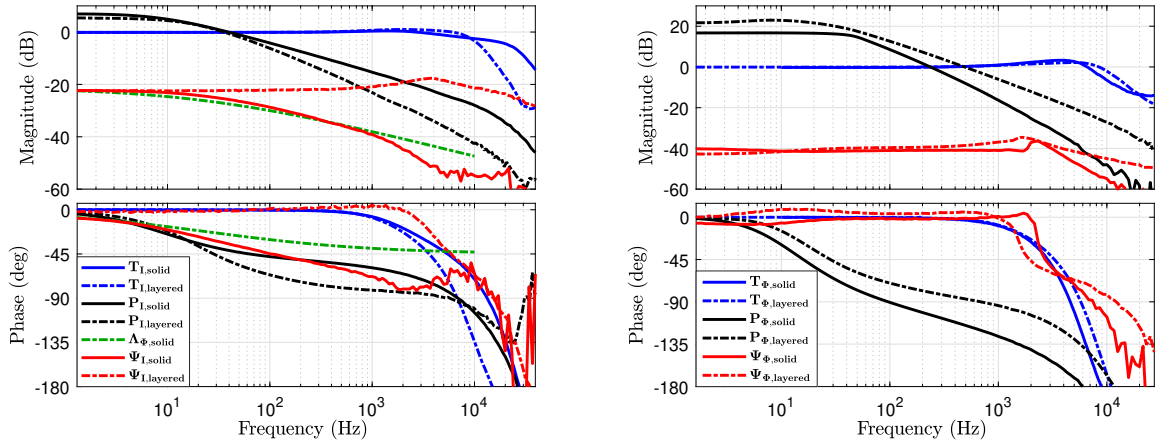
IV. CONTROL DESIGN

The cascaded control structure depicted in Fig. 2 is chosen for the system, consisting of an inner current or flux control loop and an outer position control loop. An position control bandwidth of 800 Hz is targeted to demonstrate flux control with solid core actuators beyond the system's suspension mode at 193 Hz. In order to reject disturbances in the inner loop before they can propagate to the outer control loop, the control bandwidth of the inner loop should be set about 10 times higher [24].

For the measured transfer functions $P_{I,\text{layered}}(s)$ and $P_{I,\text{solid}}(s)$, current controllers

$$C_I = k_p + \frac{k_i}{s} \quad (14)$$

with appropriate gains k_p and k_i are designed to guarantee zero steady-state error at low frequencies and reach the targeted cross-over frequency of 8 kHz [2]. The resulting closed-loop transfer functions $T_{I,\text{solid}}$ and $T_{I,\text{layered}}$ are depicted in Fig. 4a. In the layered core actuator, the measured flux $\Psi_{I,\text{layered}}$ in the air gap shows an almost constant magnitude up to several kHz,



(a) Comparison of current-controlled actuators.

(b) Comparison of flux-controlled actuators.

Fig. 4: Comparison between current-controlled and flux-controlled solid-yoke and laminated-yoke HRAs, respectively. The bode plots are measured from the current and flux reference $U_{ref,I}$ and $U_{ref,\Phi}$ to the respective output signals. T_I and T_Φ show the closed-loop transfer functions while P_I and P_Φ denote the measured plants without active control. The solid core actuator is unable to generate constant flux for higher driving frequencies due to eddy current diffusion. At around 10 Hz the flux density magnitude shows a slope of -10 dB/dec, which is modelled by $\Lambda_{\Phi,solid}$. (b) With active flux control the control input captures the effects of eddy currents, resulting in a relatively constant flux magnitudes up to 3 kHz for both actuators, shown by the air gap measurements $\Psi_{\Phi,solid}$ and $\Psi_{\Phi,layered}$.

as yoke lamination limits eddy current diffusion. In the solid core, eddy currents impair the flux generation at frequencies beyond 10 Hz, as shown by $\Psi_{I,solid}$, featuring a -10 dB/dec slope, corresponding to the measured plant $P_{I,solid}(s)$ and the flux model $\Lambda_{\Phi,solid}$.

In order to overcome these limitations, the flux measurement of the search coil is used as control input, as illustrated in Fig. 2. Transfer functions $P_{\Phi,layered}(s)$ and $P_{\Phi,solid}(s)$ are measured from U to U_{fusion} for both actuators, respectively, and depicted in Fig. 4b. Flux controllers are designed to

$$C_{\Phi,layered} = k_p + \frac{k_i}{s} \quad (15)$$

$$C_{\Phi,solid} = k_p + \frac{k_i}{s} + k_d \frac{s}{T_f s + 1}. \quad (16)$$

For the solid core flux controller, a derivative term with $T_f = 1.989 \times 10^{-5}$ and $k_d = 8.442 \times 10^{-4}$ is necessary to compensate for the additional phase lag caused by eddy currents and to ensure a sufficient phase margin at the targeted crossover frequency. The measured complementary sensitivity functions $T_{\Phi,solid}$ and $T_{\Phi,layered}$ are depicted in Fig. 4b. The parameters for all four controllers and the gain and phase margins of the corresponding open-loop transfer functions are listed in Tab. II.

Air gap measurements $\Psi_{\Phi,solid}$ and $\Psi_{\Phi,layered}$ are carried out to investigate the potential dynamic improvements gained through flux control. Consequently, both actuator types show a relatively constant flux generation up to around 3 kHz.

A. Position control

The mover dynamics are investigated for both control schemes by measuring the position with the interferometric sensor.

Frequency response functions are measured from the power amplifier's reference input U to the interferometer's position signal output U_{pos} and shown in Fig. 5. A shift of the first

TABLE II: Inner loop controller parameters for both actuators with gain and phase margins.

	$C_{I,solid}$	$C_{I,layered}$	$C_{\Phi,solid}$	$C_{\Phi,layered}$
k_p	21.877	70.794	46.901	6.309
k_i	2.749×10^5	4.448×10^5	1.122×10^5	3.964×10^4
GM	11.2 dB	16.3 dB	6.2 dB	12 dB
PM	60°	52°	35°	47°

mechanical resonance from 175 Hz to 193 Hz can be observed for both actuator types, if the control mode is switched from current to flux control. This is caused by a change in the mover's operating point, leading to a changed effective stiffness due to the switch from the current monitor to the fused sensor signal.

With current control, the impact of eddy currents in the solid iron yoke stands out and shows in an additional 41° phase lag at the suspension mode of $G_{I,solid}$ when compared to $G_{I,layered}$, while with rising frequency the phase lag further increases. This renders a position control bandwidth above the system's suspension mode infeasible.

With implemented flux control, the phase lag resulting from eddy currents does not show up at low frequencies in $G_{\Phi,solid}$, essentially showing a similar behaviour as the current-controlled layered core actuator. With flux control, the layered core shows a phase lead of 12° when compared to $G_{I,layered}$. This means that the implemented flux controllers effectively compensate the impacts of eddy currents in both yoke configurations and enable the integration of an outer control loop for

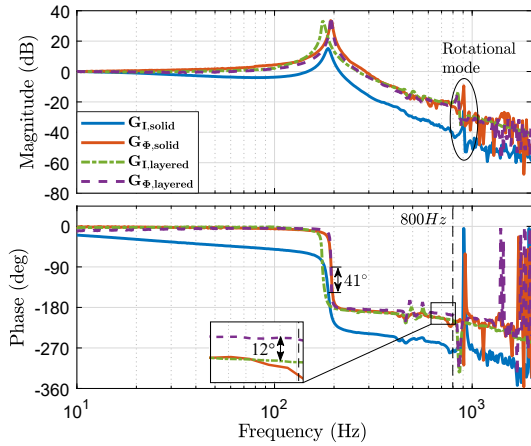


Fig. 5: Comparison of mover dynamics with flux and current control used for layered and solid core actuators, respectively. The bode plots are measured from the references $U_{ref,I}$ and $U_{ref,\Phi}$ to the position signal U_{pos} . The plant $G_{I,solid}$ shows a considerable phase lag of 41° compared to $G_{I,layered}$, which in turn shows an additional phase lag of 12° compared to $G_{\Phi,layered}$.

TABLE III: Model parameters for the current-controlled solid core and the layered core HRA.

	Solid core	Layered core
K_s	0.224 61	0.9577
ω_r	$2\pi \cdot 1200$ rad/s	$2\pi \cdot 1572$ rad/s
ω_0	$2\pi \cdot 193.4$ rad/s	$2\pi \cdot 178.6$ rad/s
ξ	0.0135	0.01
d_1	57.68	109.3
d_2	57.88	109.7
k_1	3.327×10^7	2.098×10^7
k_2	3.219×10^7	2.852×10^7

position control.

In the next step, the state-of-the-art current-controlled layered core actuator and the experimental flux-controlled solid core actuator are compared by implementing position control using H_∞ control synthesis.

In order to enable an optimal controller synthesis, the corresponding transfer functions are modelled to

$$M = K \frac{-\frac{s}{\omega_r} + 1}{\frac{s^2}{\omega_0^2} + 2\xi\frac{s}{\omega_0} + 1} \frac{s^2 + d_1s + k_1}{s^2 + d_2s + k_2}, \quad (17)$$

with the parameters listed in Tab. III. The additional 2^{nd} -order transfer function is added to consider the resonance-antiresonance pair at 900 Hz due to an excitation of a rotational mode. The system of the layered yoke, $G_{I,layered}$, deviates slightly and shows additional small antiresonance-resonance combinations at 450 Hz and 550 Hz, which may originate from manufacturing tolerances. The objective of robust control is to find a controller $C_x(s)$, which stabilizes the closed-loop system, tracks the reference, attenuates disturbances, rejects measurement noise and saves control energy [24]. The control

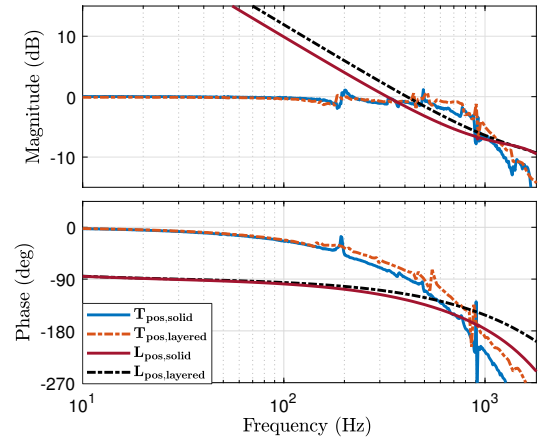


Fig. 6: Complementary sensitivity functions of the outer position control loop for the flux-controlled solid core and the current-controlled layered core actuator types, reaching a bandwidth of 750 Hz and 790 Hz, respectively.

TABLE IV: Weighting function parameters for both actuators.

Parameter	Value	Parameter	Value
ω_{s1}	$2\pi \cdot 700$ rad/s	ω_{s2}	$2\pi \cdot 1$ rad/s
ω_{t1}	$2\pi \cdot 1 \times 10^3$ rad/s	ω_{t2}	$2\pi \cdot 1 \times 10^5$ rad/s
ω_{u1}	$2\pi \cdot 700$ rad/s	ω_{u2}	$2\pi \cdot 7 \times 10^6$ rad/s

requirements can be formulated as an optimization problem

$$\min \left\| \begin{bmatrix} W_S S \\ W_U U \\ W_T T \end{bmatrix} \right\|_\infty \quad (18)$$

with the sensitivity function S , the input sensitivity function U and the complementary sensitivity function T . Essentially, the H_∞ -norm of these sensitivities is minimized, while a stabilizing controller C_x is iteratively determined. Frequency-dependent weighting functions W_S , W_U and W_T are used to limit and shape the frequency behaviour and reflect the design objectives. W_S imposes limits on S at low frequencies to ensure sufficient disturbance attenuation. The second weighting function W_U is used for shaping the frequency behaviour of the input sensitivity function and is limiting the control action at high frequencies. In order to demonstrate the position control capabilities above the system's natural frequency, a control bandwidth of 800 Hz is targeted. The weighting functions are chosen to

$$W_S = 0.1 \frac{s + \omega_{s1}}{s + \omega_{s2}} \quad (19)$$

$$W_U = 10^{-4} \frac{\omega_{u2}^2 s^2 + 1.4 \cdot \omega_{u1} s + \omega_{u1}^2}{\omega_{u1}^2 s^2 + 1.4 \cdot \omega_{u2} s + \omega_{u2}^2} \quad (20)$$

$$W_T = \frac{1}{5} \frac{\omega_{t2}^2 s^2 + 1.4 \cdot \omega_{t1} s + \omega_{t1}^2}{\omega_{t1}^2 s^2 + 1.4 \cdot \omega_{t2} s + \omega_{t2}^2} \quad (21)$$

for both actuators, with the listed parameters in Tab. IV. The H_∞ -synthesis is carried out in Matlab using the derived models (see Eq. 17), which results in two controllers $C_x(s)$ of 9^{th} order.

V. EXPERIMENTAL RESULTS

In order to evaluate the control performance, complementary sensitivity functions $T_{pos,solid}$ and $T_{pos,layered}$, depicted in Fig. 6, are measured for the current-controlled layered core actuator and for the flux-controlled solid core. The bode plot is measured from the reference input $U_{ref,pos}$ to the interferometer output U_{pos} with active position control.

The simulated open-loop transfer function $L_{pos,solid}$ shows a phase margin of 55° and a gain margin of 8.4 dB at a cross-over frequency of 360 Hz. For the layered core, $L_{pos,layered}$ shows a phase margin of 59° and a gain margin of 7.2 dB at 410 Hz. The difference in the 0-dB crossing line results from the difference in the models used for both actuators. However, a similar control performance is reached for both actuator types, with a -3 dB-bandwidth of about 750 Hz for the solid core and 790 Hz for the layered core.

In summary, four HRA configurations are analysed, where the implementation of flux control for the solid core HRA allows for extending the positioning bandwidth by about one decade compared to current control. In case of the layered core HRA, a high positioning bandwidth can be achieved with both controllers, with flux control showing an improved phase behaviour by capturing the impact of eddy current formation.

VI. CONCLUSION

This paper analyses the dynamic properties of applied flux and current control for a solid core and a laminated core HRA. The implementation of flux control for HRAs with a solid iron yoke shows that the phase lag due to eddy currents can be reduced by 41° at the system's suspension frequency when compared to conventional current control. The comparison with a current-controlled layered core actuator of the same geometry shows that flux control offers the possibility to dispense yoke layering in favour of an increased fill factor. Flux control in combination with a layered core HRA shows an mitigation of the phase lag by 12° near the targeted position control bandwidth compared to current control. Essentially, both actuators show comparable dynamics in the frequency domain if the appropriate controllers are implemented.

The applied position controller further highlights these findings by showing that similar closed-loop position control bandwidths of 750 Hz for the flux-controlled solid core HRA and 790 Hz for the current-controlled laminated core HRA can be achieved.

While the flux-controlled laminated core actuator is clearly superior in terms of efficiency, the findings suggest that the flux-controlled solid core HRA can be utilized for applications where yoke lamination is deemed difficult. Future work includes the comparison and evaluation of the force dynamics and energy consumption of both actuator types [25].

REFERENCES

- [1] Z. Zhang, H. Zhou, and J.-a. Duan, "Design and analysis of a high acceleration rotary-linear voice coil motor," *IEEE Transactions on Magnetics*, vol. 53, no. 7, pp. 1–9, 2017.
- [2] R. M. Schmidt, G. Schitter, A. Rankers, and J. Van Eijk, *The Design of High Performance Mechatronics: High-Tech Functionality by Multidisciplinary System Integration*, 2nd ed. IOS Press, 2014.
- [3] D. Kang, K. Kim, D. Kim, J. Shim, D.-G. Gweon, and J. Jeong, "Optimal design of high precision xy-scanner with nanometer-level resolution and millimeter-level working range," *Mechatronics*, vol. 19, no. 4, pp. 562–570, 2009.
- [4] Q. Xu, "Design and implementation of a novel rotary micropositioning system driven by linear voice coil motor," *Review of Scientific Instruments*, vol. 84, no. 5, p. 055001, May. 2013.
- [5] E. Csencsics and G. Schitter, "System design and control of a resonant fast steering mirror for lissajous-based scanning," *IEEE/ASME Transactions on Mechatronics*, vol. 22, no. 5, pp. 1963–1972, 2017.
- [6] D. Wertjanz, E. Csencsics, and G. Schitter, "3 dof vibration compensation platform for robot-based precision inline measurements on free-form surfaces," *IEEE Transactions on Industrial Electronics*, pp. 1–1, 2021.
- [7] D. B. Hiemstra, G. Parmar, and S. Awtar, "Performance tradeoffs posed by moving magnet actuators in flexure-based nanopositioning," *IEEE/ASME Transactions on Mechatronics*, vol. 19, pp. 201–212, 2014.
- [8] N. H. Vrijsen, J. W. Jansen, and E. A. Lomonova, "Comparison of linear voice coil and reluctance actuators for high-precision applications," in *Proceedings of 14th International Power Electronics and Motion Control Conference EPE-PEMC 2010*, pp. S3–29–S3–36, 2010.
- [9] A. Katalenic, H. Butler, and P. P. J. van den Bosch, "High-precision force control of short-stroke reluctance actuators with an air gap observer," *IEEE/ASME Transactions on Mechatronics*, vol. 21, no. 5, pp. 2431–2439, 2016.
- [10] E. Csencsics, J. Schlarp, and G. Schitter, "High-performance hybrid-reluctance-force-based tip/tilt system: Design, control, and evaluation," *IEEE/ASME Transactions on Mechatronics*, vol. 23, no. 5, pp. 2494–2502, 2018.
- [11] D. Wu, X. Xie, and S. Zhou, "Design of a normal stress electromagnetic fast linear actuator," *IEEE Transactions on Magnetics*, vol. 46, no. 4, pp. 1007–1014, 2010.
- [12] S. Ito, B. Lindner, and G. Schitter, "Sample-tracking vibration isolation with hybrid reluctance actuators for inline metrology," *IFAC-PapersOnLine*, vol. 52, no. 15, pp. 537–542, 2019.
- [13] S. Ito, F. Cigarini, and G. Schitter, "Flux-controlled hybrid reluctance actuator for high-precision scanning motion," *IEEE Transactions on Industrial Electronics*, vol. 67, no. 11, pp. 9593–9600, Nov. 2020.
- [14] E. Csencsics, J. Schlarp, and G. Schitter, "Bandwidth extension of hybrid-reluctance-force-based tip/tilt system by reduction of eddy currents," in *2017 IEEE International Conference on Advanced Intelligent Mechatronics (AIM)*, pp. 1167–1172, 2017.
- [15] S. K. Mukerji, M. George, M. B. Ramamurthy, and K. Asaduzzaman, "Eddy currents in solid rectangular cores," vol. 7, pp. 117–131, 2008.
- [16] R. Stegmann, S. Cabeza, M. Pelkner, V. Lyamkin, N. Sonntag, G. Bruno, B. Skrotzki, and M. Kreuzbruck, "Evaluation of high spatial resolution imaging of magnetic stray fields for early damage detection," in *AIP Conference Proceedings*, DOI 10.1063/1.4974688. Author(s), 2017.
- [17] D. J. Kluk, M. T. Boulet, and D. L. Trumper, "A high-bandwidth, high-precision, two-axis steering mirror with moving iron actuator," *Mechatronics*, vol. 22, no. 3, pp. 257–270, Apr. 2012.
- [18] F. Cigarini, S. Ito, J. Konig, A. Sinn, and G. Schitter, "Compensation of hysteresis in hybrid reluctance actuator for high-precision motion," vol. 52, no. 15, pp. 477–482, 2019.
- [19] S. Ito, S. Troppmair, F. Cigarini, and G. Schitter, "High-speed scanner with nanometer resolution using a hybrid reluctance force actuator," vol. 8, no. 2, pp. 170–176, 2019.
- [20] D. Zhang, "Magnetic skin effect in silicon-iron core at power frequency," *Journal of Magnetism and Magnetic Materials*, vol. 221, no. 3, pp. 414–416, 2000.
- [21] V. Moroz, D. Calus, and O. Makarchuk, "Fractional order transfer function for eddy current simulation," in *2018 14th International Conference on Advanced Trends in Radioelectronics, Telecommunications and Computer Engineering (TCSET)*. IEEE, 2018.
- [22] J. A. T. Machado and A. M. S. F. Galhano, "Fractional order inductive phenomena based on the skin effect," *Nonlinear Dynamics*, vol. 68, no. 1–2, pp. 107–115, Sep. 2011.
- [23] J. Feeley, "A simple dynamic model for eddy currents in a magnetic actuator," *IEEE Transactions on Magnetics*, vol. 32, DOI 10.1109/20.486532, no. 2, pp. 453–458, 1996.
- [24] K. Zhou and J. C. Doyle, *Essentials of Robust Control*. Prentice-Hall, 1998.
- [25] C. Haider, E. Csencsics, and G. Schitter, "Frequency-dependency of force dynamics of hybrid reluctance actuators," in *IEEE/ASME International Conference on Advanced Intelligent Mechatronics (AIM)*, 2024. Accepted.